Satellite Microphysical Retrievals for Land-Based Fog with Validation by Balloon Profiling

MELANIE A. WETZEL, RANDOLPH D. BORYS, AND LING E. XU*

Atmospheric Sciences Center, Desert Research Institute, Reno, Nevada

(Manuscript received 24 May 1995, in final form 3 October 1995)

ABSTRACT

Digital data from the National Oceanic and Atmospheric Administration Advanced Very High Resolution Radiometer (AVHRR) satellite instrument provides multispectral images in visible near-infrared and thermal infrared wave bands, which have been utilized to develop retrieval techniques for estimating the droplet effective radius and optical depth of land-based fog. The retrieval methods are based on multiple scattering calculations that simulate the increased near-infrared absorption by fog layers with increasing droplet size and liquid water path. The AVHRR thermal window channels are utilized to remove the effects of thermal emission in the near-infrared band.

New instrumentation and field sampling methods have been developed for obtaining detailed vertical profiles of fog droplet size distributions and thermodynamic conditions in fog decks. The in situ measurements derived from the field observations were employed to test the satellite retrieval techniques. Intercomparison shows a close correspondence between field observations and retrieved values of the fog droplet effective radius as well as fog optical depth. Simulated 4-km near-infrared and visible pixel data are also used to test retrievals from *GOES-8*. The AVHRR and *GOES-8* retrievals provide a mapped database of the fog microphysical and depth parameters over the entire region of fog, which may be applied to numerical simulation of fog evolution and pollutant deposition, nowcasting of fog visibility hazards, and global monitoring of fog influences on the atmosphere–surface radiation budget.

1. Introduction

The analysis of fog conditions on short timescales (nowcasting and mesoscale forecasting) should provide information on the geographic distribution as well as the physical structure of fog. Both in situ measurements and satellite observations (Welch and Wielicki 1986) of fog indicate considerable local structure, including mesoscale variations in droplet size and optical depth, which may be used to indicate evolutionary stage and mixing processes. Measurements of many fog droplet size spectra by Tonna (1989) suggest that fog types (valley, advection, and radiation fogs) have characteristic size distributions, which would lead to differences in physical processes such as droplet settling speed and in-fog impacts such as visual range. Results of detailed numerical models for fog evolution (Welch et al. 1986; Bott et al. 1990; Duynkerke 1991) demonstrate the need for observations of droplet size and liquid water path/optical path conditions for model initialization, updating, and validation. Applied models such as that of Pandis and Seinfeld (1989), which predicts acid deposition by fog, would also benefit from assimilating observations of droplet size, in this case to specify droplet settling speed (vertical mass flux).

After initial air-layer saturation and fog formation, the factors that influence subsequent fog development and dissipation include (a) fog optical depth (in the longwave, for infrared transmittance and emittance; in the shortwave, for penetration of solar flux), (b) proximity to fog edge or topographic contours (which allow lateral mixing and constrain airflow), and (c) fog droplet size (which influences droplet growth rates, evaporation at lateral boundaries, gravitational settling, and radiative exchange). Satellite remote sensing techniques can be used to provide information related to each of these factors.

Mapping fog distribution with satellite image data allows identification of surface influences on fog structure. Lee (1987) provided examples of California Central Valley fog in which fog over urban centers was observed to dissipate more quickly and completely than fog over the adjacent rural areas. Thus, mapping of fog extent provides phenomenological estimates of fog life cycle. These observations also demonstrate the importance of numerical simulation models, which accurately account for radiative transmittance by the fog droplet population. The models are driven by assumed

* Current affiliation: Information Processing System of California, Inc., Belmont, California.

Corresponding author address: Dr. M. Wetzel, Desert Research Institute, P.O. Box 60220, 5625 Fox Avenue, Reno, NV 60220.
E-mail: wetzel@sage.dri.edu

or observed conditions of fog droplet size distribution and fog vertical structure, as well as conditions of surface temperature and soil moisture. The vertical extent of horizontally uniform fog can be estimated by geographic mapping, using graphic overlay or automated matching of topographic contour levels to the fog boundary. Development of time-composited satellite image data for fog events can further be used to evaluate fog diurnal cycles during various synoptic and surface conditions.

Satellite-derived information on fog radiance in narrow spectral bands can provide information on the equivalent blackbody temperature of the fog layer as well as, during daylight, the shortwave reflectance due to microphysical characteristics of the fog. Estimation of fog droplet size could be directly applied to numerical or conceptual models of fog evolution, since droplet size influences the longwave and shortwave net flux and heating/cooling rates within the vertical profile of the fog. Fog droplet size also can be used to evaluate the presence of aerosol in the boundary layer. While the albedo of fog is less susceptible than stratus cloud to changes in aerosol concentration (Platnick and Twomey 1994), the initial formation, persistence, and recurrence of fog can be significantly influenced by local aerosol–fog interactions. Fog can increase the concentration of sulfate aerosol as a result of aqueous-phase production through oxidation by H_2O_2 (Pandis et al. 1990), then can lead to net sulfate deposition if H_2O_2 becomes locally depleted. In addition, the aerosol size, which is related to aerosol source composition, has been shown to influence the width of the fog droplet size distribution (Wobrock et al. 1986). Each of these fog–aerosol interactions may alter the growth time and settling of fog droplets, which in turn play a role in fog radiative budget as well as the manifestation of fog effects in terms of visibility and pollutant deposition. Simultaneous estimation of fog droplet size with the vertical and optical depths of the fog layer could be applied to a more complete interpretation and model implementation for predicting the subsequent fog evolution.

This paper describes the development and testing of algorithms for deriving fog droplet size, optical depth, and physical depth over land surfaces from multispectral National Oceanic and Atmospheric Administration (NOAA) Advanced Very High Resolution Radiometer (AVHRR) imagery. Retrieval algorithms for stratiform cloud have been developed from multispectral radiative modeling (Wetzel and Vonder Haar 1991). The ability of this method was demonstrated by Wetzel and Vonder Haar (1990, 1991), using model sensitivity studies and low-altitude airborne spectral radiometer measurements. Another previous study of estimating droplet size from aircraft radiometer data indicated a bias toward overestimation (Nakajima et al. 1991), but these may have been influenced by incorrect water vapor transmittance calculations in the path between cloud top and the aircraft sensor (Taylor 1992). More recent analyses suggest that stratocumulus droplet size and optical depth estimates are generally within the range of certainty for corresponding in-cloud measurements by optical probe instruments (Platnick and Valero 1995).

It is difficult to obtain microphysical measurements in fog or stratus cloud over land by aircraft sampling, due to flying restrictions. A new field method has been established for obtaining in situ measurements of near-surface cloud microphysical and thermodynamic parameters. Sampling of boundary layer fog is accomplished by use of a tethered balloon, which carries a cloud droplet imaging system and an airsonde package for obtaining thermodynamic variables. Analysis of the data provides thermodynamic and microphysical characterization of fog layers sampled during the times of satellite overpasses. Simultaneous digital image data from the NOAA AVHRR provide the radiances needed to implement and test cloud parameter retrieval algorithms developed from radiative transfer theory. Figure 1 shows a schematic diagram of the observational objectives. The current study presents the development and validation of a satellite retrieval method for the microphysical characteristics of land-based fog.

2. Numerical modeling of cloud spectral reflectance

The development of an operational retrieval method for cloud microphysical and optical characteristics requires the application of a numerical model for cloud spectral radiance, due to the high spectral variability of cloud scattering and absorption characteristics as functions of cloud particle size distribution and optical depth, as well as the atmospheric composition external to the cloud. A multiple-scattering radiative transfer model known as the "discrete ordinates method" (DISORT) has been applied to this research. The model

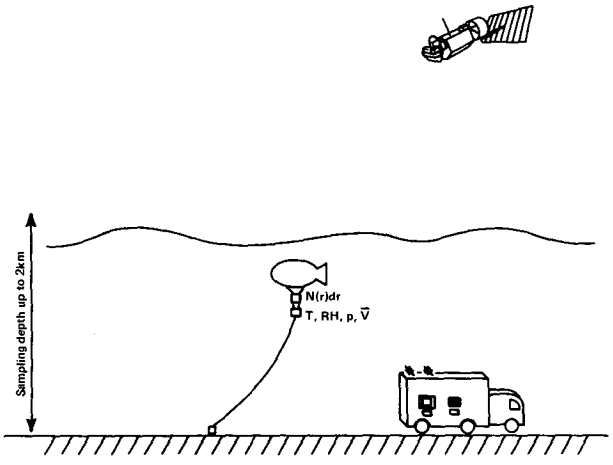

FIG. 1. Schematic diagram of the field observations taken for use in the validation of AVHRR retrieval algorithms.

allows the direct representation of stratiform cloud with multiple plane-parallel layers (Stamnes et al. 1988; Tsay et al. 1990). In the discrete ordinates model, the integral form of the monochromatic radiative transfer equation is approximated by a finite sum of terms representing a prespecified vector of directions of radiation streams. The atmosphere can be vertically inhomogeneous and nonisothermal in character. Both azimuthal and zenithal expansions of terms are followed, and the scattering phase function is treated numerically as a Legendre polynomial expansion. The depths of individual model layers are selected such that each is sufficiently homogeneous to have a constant scattering phase function and single-scattering albedo. A set of algebraic linear equations are developed, which are solved for homogeneous layers and then for the combined layer system. Gaussian or Lobatto quadrature rules are used for the numerical integration steps (Stamnes and Swanson 1981).

The method by which the theoretical radiance results were used was to perform DISORT calculations a priori for a wide range of observation and solar angles, a range of droplet size distribution types, and a range of cloud optical depths. Second, the relationship between spectral reflectances for AVHRR channels 1 and 3, centered at wavelengths of 0.65 and 3.75 μm, respectively, were used to interpolate the observations to the model simulation results. These model results vary with solar zenith angle and satellite viewing angle and demonstrate a distinct variation in near-infrared cloud reflectance as a function of droplet size. Figure 2 depicts the relationship of bispectral reflectances for varying droplet populations. The droplet size distribution is characterized by the modified gamma distribution function and the effective radius for that function given a specified liquid water concentration. The droplet effective radius for a population of spherical droplets is

$$r_e = \frac{\int r^3 n(r)\,dr}{\int r^2 n(r)\,dr}. \qquad (1)$$

Values of zero surface albedo in each channel are used in Fig. 2 only for reference to an idealized cloud layer. Land or water surface albedo values are generally 0.03–0.25 in AVHRR channel 1 and 0.01–0.10 in channel 3 and can be estimated from the satellite observations, which are corrected for atmospheric attenuation and path radiance. Exceptions occur in limited areas of sun glint from water surfaces, where reflectance in each of these channels can be much higher and satellite retrievals are not possible. Figure 2 also provides an indication of the region of "overlap" of the model curves for small optical depths. Both the effects of nonzero surface reflectance and overlapping bispectral reflectances reduce the ability to retrieve droplet size from optically thin clouds. The particular limitation is case dependant and must be evaluated by preparing model curves similar to those in Fig. 2, with locally specific surface albedo conditions. The conditions relevant to the present case study are discussed in section 5.

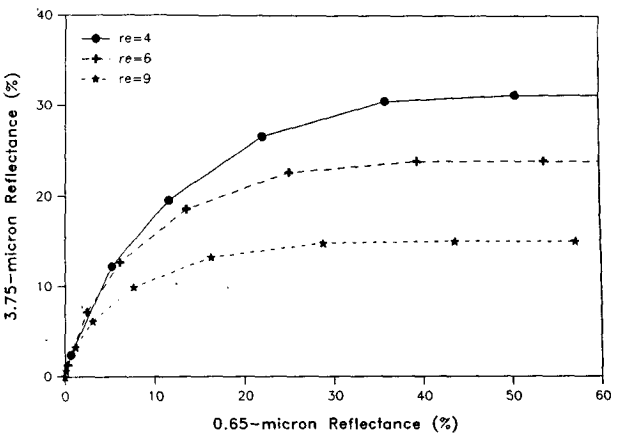

FIG. 2. Bispectral reflectances calculated for cloud layers of effective radius r_e equal to 4, 6, and 9 μm, over a surface with zero albedo at both the 0.65- and 3.75-μm wavelengths. The solar zenith angle is 68°, satellite zenith angle is 15°, and sun–satellite relative azimuth angle is 90°.

The analysis methodology for the satellite retrieval of fog microphysical parameters is based on the use of the model calculations of fog-layer spectral radiance for the central wavelengths representing the AVHRR multichannel image data. Fitting of the observed cloud reflectances to results of the multiple-scattering radiation model at the appropriate solar and viewing geometries is accomplished by use of spline interpolation. In this procedure, we estimate both cloud optical depth and effective droplet radius. A geographic database is used to store the latitude and longitude coordinates of each pixel's input channel radiances and output fog parameters. The database can be resampled to any map projection and map scaling factor.

Certain case-specific input parameters are needed for the DISORT model application. Surface albedo values were produced from satellite shortwave channel data close to the fog area, while fog-top temperature was derived from the satellite thermal channel. Atmospheric extinction and path radiance parameters were obtained by methods discussed in section 5.

3. Field sampling methods

The in situ sensing of fog microphysical parameters was necessary to accomplish the goals of this research. Measurements of cloud microphysical properties are often made from aircraft equipped with the Particle Measurement Systems, Inc. (PMS) forward-scattering spectrometer probe (FSSP) and other optical probes to obtain droplet size spectra. These devices, however,

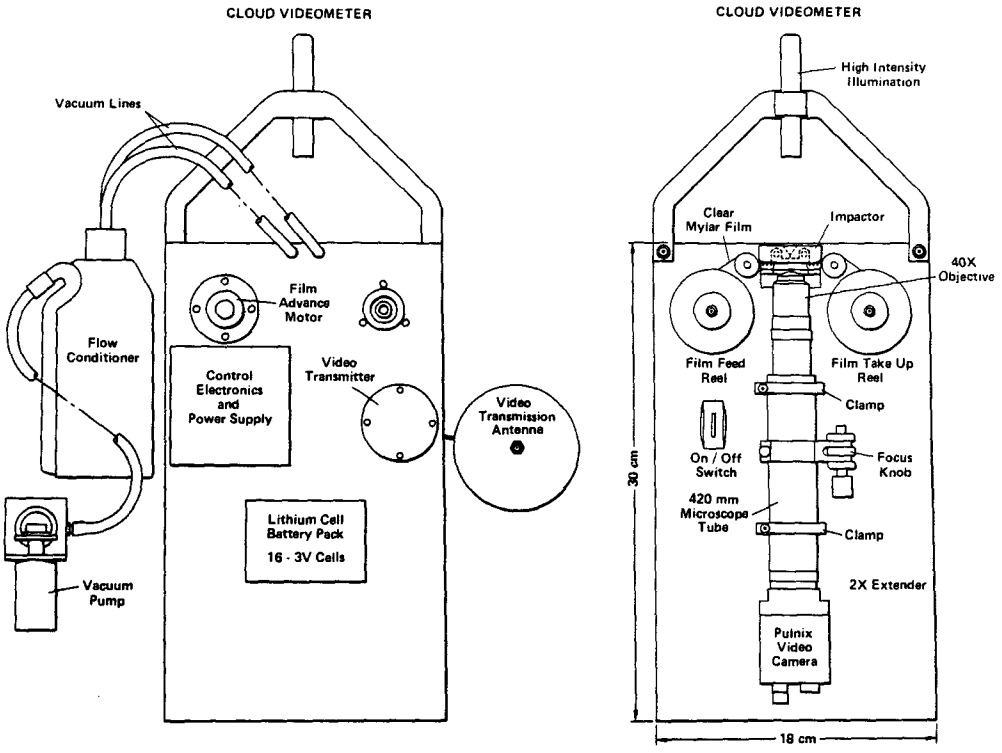

FIG. 3. Schematic diagram of the front and back of the CDV drawn to scale. Overall dimensions of the base plate are 30 cm × 18 cm × 8 cm deep.

have limited operational characteristics. They generally require a large amount of power and must be mounted on a platform with sufficient payload capacity to carry the large weight of their combined data system and sensor package. Operational limitations due to Federal Aviation Administration regulations disallow the use of aircraft in restricted visibility conditions at altitudes below 1200 ft (366 m) above ground level (AGL). In fact, most land-based fog layers are too shallow to be adequately sampled by aircraft. A cloud droplet sonde was developed that was deployed from the ground using a tethered balloon system, thus avoiding the need of an aircraft.

a. The DRI Cloud Droplet Videometer

The recently developed Desert Research Institute (DRI) Cloud Droplet Videometer (CDV) system consists of an aspirated cloud droplet impactor, a clear Mylar film supply for the impaction surface, a 420-mm microscope with a 40× objective and a 2× extender focused to the impaction surface and attached to a CCD videocamera, timing electronics to move the Mylar film and provide a fresh impaction surface, a miniature video transmitter, and a 12-V dc power supply. Continuous illumination was provided by a 1.5-V high-intensity focusing flashlight. The entire unit is powered by a 12-V battery pack composed of 3-V lithium battery cells. The current CDV is built on an aluminum plate. Figure 3 is a diagram of the front and back view of the CDV layout. Design specifications for obtaining high collection efficiency for the range of fog droplet sizes were obtained from Marple and Willeke (1976). A 12-V dc diaphragm pump is used to draw air through the impactor. Because of the piston action of the pump, some vibration of the Mylar film occurred, causing a blurring of the video image due to both mechanical vibration and pulsation of the airstream. A small conditioning chamber was installed in the vacuum line between the pump and the impactor to alleviate this air pulsation problem. In addition, the pump was physically isolated from the optical components to eliminate the mechanical vibration. The theoretical design collection efficiency of the impactor is 100% for droplets of at least 1.6-μm diameter. The high-intensity light provides the forward-scattered light illumination through the impactor jet opening. The impactor jet diameter is 800 μm. Fresh Mylar film is drawn past the impaction point at an adjustable rate and pauses for an adjustable period.

The image of the impacted droplets viewed from the underside of the Mylar film is a circle representing the perimeter of the base of the resulting droplet cap. In order to determine the size of the original droplet, the relationship between cap diameter and original droplet

diameter must be determined. This relationship can be expressed as

$$D_d = KD_c \tag{2}$$

for the respective diameters D of the droplet (d) and cap (c), and the conversion factor K is given as function of the contact angle σ:

$$K = \frac{[(1 - \cos\sigma)(4 - 2\cos^2\sigma - 2\cos\sigma)]^{1/3}}{2\sin\sigma}. \tag{3}$$

Possible sampling errors can lead to discrepancies in the representativeness of the droplet cap diameters, due to variations in contact angle, electrostatic charging of the film, spreading of the droplets on impact, and droplet evaporation. The contact angle for pure water is specified by the composition of the solid surface. Although fog and cloud droplets can include soluble salts, in concentrations of greater than 10 ppm in some cases, their effect on the contact angle can be neglected. For instance, a 1000-ppm solution of nitric acid would increase the value of the cosine of the contact angle by only 1%. The greatest source of variability in the contact angle is contamination of the substrate surface. The film used in these experiments was "virgin" Mylar, and care was taken to eliminate contact of this surface with any other during instrument preparation. Laboratory measurements of impacted droplets using this Mylar showed contact angles to be 70.5° ± 10.5°. This range in contact angle produces an uncertainty of less than 0.5 μm in the resultant droplet diameter for a typical cap value of 10 μm.

Electrostatic charging of the Mylar film could alter the droplet impaction characteristics of the CDV. Charging of the film was minimized, as the film itself acted as a seal on the machined aluminum impactor block (see Fig. 3). This physical contact with the impactor block allowed any acquired charge to be dissipated from the film into the aluminum base plate of the instrument. Droplet spreading, which may be caused by the impact of droplets at a velocity of 25 m s^{-1}, could produce diameter overestimates. This would be most significant for droplets that are large enough for their momentum and deformation force on impact to overcome the restoring force of the droplet cap surface tension, which would be evidenced by a reduction in contact angle. Results of laboratory measurements of contact angles for droplets with a range of diameters exceeding 1 mm showed little variability in contact angle, which indicates little effect of droplet spreading on impact. Potential errors due to evaporation after contact are not significant since the CDV is operated in a saturated cloud environment. During balloon profiling in the fog, cloud top was easily identified by the sudden decimation of droplets and the accompanying drop in relative humidity measured by the airsonde unit. These time periods are excluded from the fog droplet analysis.

b. Videometer data analysis

The video image from the camera is transmitted via radio frequency to a ground receiving station consisting of a down converter and a video discriminator, with the video image recorded in real time on a super-VHS (high image resolution) tape recorder. After a sampling period, the video images are analyzed using a PC-based image analysis system coupled with a frame grabber to size and count the droplet images in each frame. The final image magnification on the video monitor is 1200×, allowing droplets of 1-μm radius to be resolved. An example of an image frame received is shown in Fig. 4. The dimensions of the image are approximately 70 μm × 60 μm. The area imaged is less than 1% of the area of the cross section of the impaction jet. The CDV in the current configuration has a weight of 2.5 kg and a maximum flight duration (determined by battery capacity) of approximately 1 h. The technical specifications for the CDV are shown in Table 1.

The postflight data analysis is accomplished using image analysis software (Optimas Bioscan). The software allows the analyst to rapidly overlay circular graphics to the imaged droplets as shown in Fig. 4. Droplet size and number are then transferred into a database for statistical summary and graphical display. The diameter of the "cap" of water measured on the Mylar film is related to the original droplet diameter by surface tension parameters. Currently, to obtain a size distribution, the individual droplet images are identified and sized manually. This is a result of the impactor surface illumination and the impactor jet and camera objective geometry. We estimate that, including analyst error, scale calibration in the imagery, and possible errors in the inference of droplet size from the observed droplet cap diameter, the uncertainty in the reported

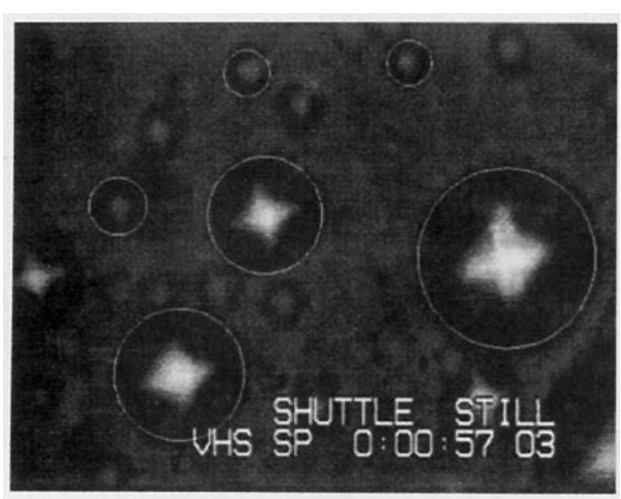

FIG. 4. Fog droplet image captured by the DRI CDV in field operation and subsequently digitized onto a PC-based image analysis system. The diameter of the largest droplet outline is 21.9 μm, while that of the smallest is 5.5 μm.

TABLE 1. DRI cloud videometer system specifications

Impactor	Jet diameter, 800 μm; jet velocity, 25 m s^{-1}; sample rate, 12.5 cm^3 s^{-1}; impaction substrate, clear Mylar film; water contact angle 70° ± 10°; pump, Spectrex AS-300 miniature precision pump with adjustable flow rate.
Microscope	80× (420-mm microscope tube fitted with 40× planar objective and a 2× C-mount extender).
Videocamera	Pulnix High-Resolution Super Mini CCD, 768(H) × 494(V), 220 mA 9–12 V dc (2.3 W)
Transmitter	Emhiser Research, Inc. 250 mW, 1687.0 MHz, 11–14 V dc, 250 mA max.
Receiver	Down East Microwave, 1650–1710-MHz loop yagi antenna, input to SDC 1691 BWP modified down converter (1680 to 1700 MHz to 70 mHz IF) to a Emhiser Research Inc. Video discriminator (video out).
Videotape recorder	JVC BR-5605UB S-VHS recorder with an RS-232C interface board.
Computer	Gateway 2000 486DX2 50-MHz VGA monitor.
Image analysis software	Optimas bioscan.

droplet diameters is less than 10%. The automation of droplet sizing is currently being developed for a second generation CDV instrument, which will reduce error and analysis time.

c. *Vertical profiling*

A tethered helium balloon served as the platform for the DRI CDV as well as for an airsonde sensor package measuring winds, dry-bulb and wet-bulb temperature, and pressure during ascent/descent sampling of fog structure. The airsonde was deployed with the CDV, also suspended below the tether balloon. The airsonde data were transmitted to a separate ground receiving antenna and data recording system as the balloon ascended/descended by winch line between the surface and fog top. The system has the capability of reaching 2 km MSL in calm wind conditions. This allowed the determination of vertical profiles of fog thermodynamic properties. The sounding profiles were used to identify the location of the temperature inversion and upper cloud boundary. These data were also utilized in verifying the cloud-top temperature retrieved from the AVHRR thermal channels.

4. Evaluation of in situ observations

a. *Cloud thermodynamic structure*

Airsonde data profiles obtained on 27 January 1993 are shown for temperatures (Fig. 5) and winds (Fig. 6), with near-calm conditions below a very slight inversion at 1017 mb and a 1.5 m s^{-1} north-northwest breeze in the upper fog portion. Cloud top and the base of a temperature inversion were observed at 1000 mb,

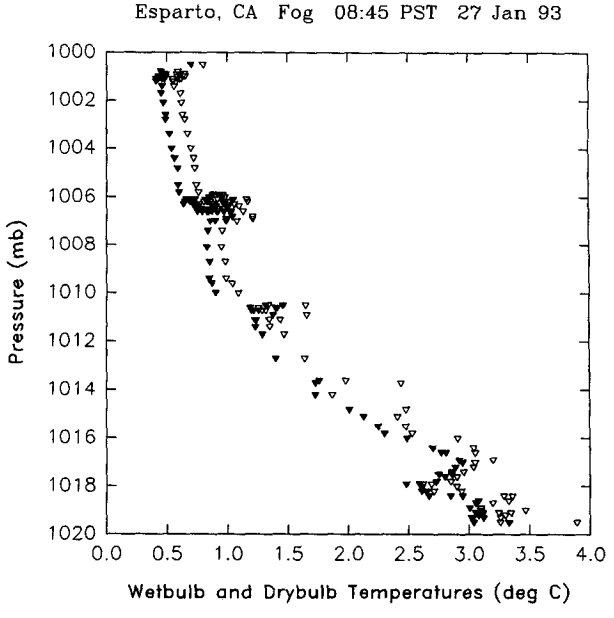

FIG. 5. Airsonde profile on 27 January 1993 for wet-bulb (filled triangles) and dry-bulb (open triangles) air temperatures. Small inversions are indicated near the surface, at 1017 mb, and at 1006 mb.

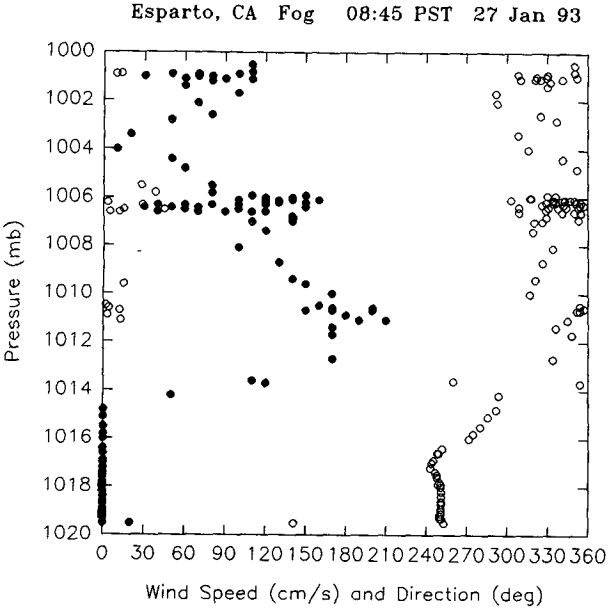

FIG. 6. Airsonde profile on 27 January 1993 for wind speed (filled circles) and wind direction (open circles).

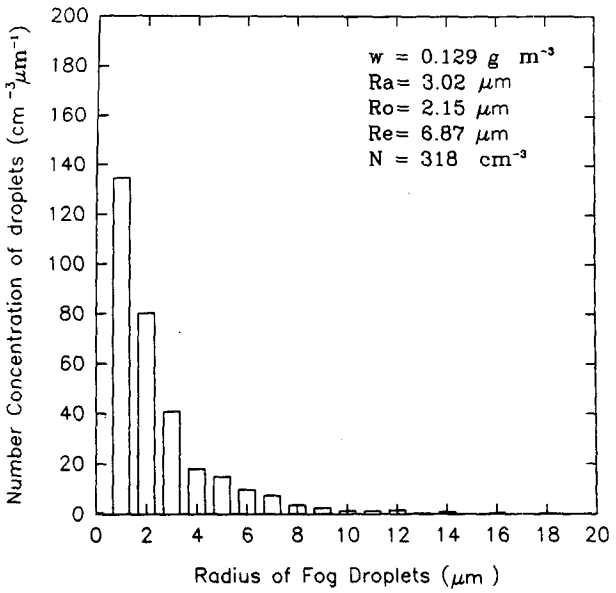

FIG. 7. Videometer analysis of fog droplet size distribution for 27 January, with values of microphysical parameters.

corresponding to a height of 201 m above ground level. The rawinsonde data from Oakland, California, for 1200 UTC also shows an inversion above approximately 1000 mb, with northerly winds there, backing to southwesterly winds above 750 mb. The rawinsonde profile is dry from 980 to 450 mb, with a thin cloud layer indicated at 440 mb (−28°C). This moist layer may be associated with the upper cloud seen to the northeast of Oakland in the satellite imagery, due to a correspondence in location as well as temperature.

b. *Droplet size distributions and optical parameters*

The DRI CDV data for the balloon ascent on 27 January is presented in Fig. 7. The droplet size distribution includes summary parameters of liquid water content w, average radius Ra, mode radius Ro and effective radius Re, and number concentration N. Total cloud depth Δz and optical depth τ calculated at a wavelength of 0.65 μm (corresponding to the central wavelength of AVHRR channel 1), are Δz = 201 m and τ = 7.0.

Droplet size distributions obtained from the CDV analysis give a vertically averaged effective droplet radius of 6.9 μm, with a number distribution that has a single mode. The majority of droplets are less than 4 μm in radius. The detection of droplets of 1-μm radius confirms the CDV design goal to sample droplets of at least 2-μm diameter. The parameter values shown in Fig. 7 are in the expected ranges for valley fog microphysical characteristics. Vertical structure within the fog was evaluated by sampling the data obtained in four vertical sublayers of approximately equal depth. The sublayer average values of liquid water content, droplet size, and optical depth are shown in Table 2. Liquid water content is relatively low (w = 0.9–1.1 g m^{-3}), except in layer 2 (0.26 g m^{-3}), which is located in the height range 58–125 m AGL. Droplet sizes (average and effective radius values) are vertically homogeneous, with a slight decrease near cloud top.

5. Satellite analysis and retrievals

This study included the collection of both field measurements and remote sensing observations of multiple fog events. We obtained AVHRR multispectral satellite data for morning overpasses, but overpass time was often too early for sufficient solar illumination. Solar flux values drop below 17% of nadir value for zenith angles greater than 80°, and images obtained for these low sun angles did not provide sufficient contrast to indicate cloud structure. This is a limitation with the current operational schedule of the morning NOAA polar orbiters. In addition, the opportunity to capture fog cases without the presence of intervening upper-level clouds was limited by the occurrence of several major cloud systems during the winter field program. The availability of *GOES-8* and *GOES-9* multispectral imagery at improved spatial and temporal resolution will contribute to the development and operational implementation of fog remote sensing in the future.

a. *Processing and calibration of AVHRR imagery*

The raw NOAA High Resolution Picture Transmission (HRPT) format AVHRR and *TIROS-N* (Television and Infrared Observation Satellite) Operational Vertical Sounder (TOVS) datasets were obtained for the 27 January 1993 case study and were analyzed using the TeraScan software developed by SeaSpace Corporation. Data were obtained from SeaSpace as well as the Scripps Satellite Oceanography Facility. At the Desert Research Institute, the five-channel AVHRR digital data were calibrated, and interactive pixel navigation correction was made using visual landmarks in the region. The values of AVHRR pixel brightness were calculated as percentage equivalent albedo values for channel 1 (0.58–0.68 μm) and channel 2 (0.725–1.10 μm) and as equivalent blackbody temperatures in channels 3 (3.55–3.93 μm), 4 (10.30–11.30 μm), and 5 (11.50–12.50 μm). The derivation of satellite nar-

TABLE 2. Fog-layer microphysical parameters

Layer	Base (m)	Depth (m)	w (g m^{-3})	r_a (μm)	r_e (μm)	τ
1	0	58	0.11	2.9	6.9	1.5
2	58	67	0.26	3.7	7.5	3.8
3	125	42	0.09	2.8	6.9	0.9
4	167	34	0.08	2.7	5.6	0.8

rowband spectral radiance L_{sat} (W m^{-2} μm^{-1} sr^{-1}) from the albedo A (%) values follows

$$L_{sat} = \frac{Af}{100w\pi}, \quad (4)$$

where f represents the portion of shortwave broadband flux used in the laboratory calibration for the AVHRR instrument, weighted by the channel response function, and w is the equivalent width of the channel response function (Kidwell 1991). The equivalent blackbody temperature values are derived from temperature-specific channel calibration coefficients for each of the infrared channels, including the near-infrared channel 3. These were converted to Planck blackbody spectral radiances based on channel response functions.

The LOWTRAN7 atmospheric transmittance code (Kneizys et al. 1988) was used to produce optical path correction values for AVHRR channel radiances. An equation that represents the satellite-viewed radiance in terms of the target radiance L_{tar}, atmospheric transmittance T_{atm}, and atmospheric path radiance L_{path} is

$$L_{sat} = L_{tar}T_{atm} + L_{path}. \quad (5)$$

The retrieval requires the interpolation of observed cloud reflectances in AVHRR channels 1 and 3 to families of reflectance curves derived from the discrete ordinates model. Therefore, the cloud-top reflectances must be estimated from the satellite-observed radiances. Cloud-top reflectance R (%) can be expressed as

$$R = \frac{100\pi L_{tar}}{\mu_0 E_0 + D}, \quad (6)$$

where μ_0 is the cosine of the solar zenith angle, E_0 is the calculated downward direct solar flux (W m^{-2} μm^{-1}), and D is the downward diffuse flux. The downward diffuse component is significant in conditions of low sun angle and/or haze scattering.

In the case of channel 3 target radiance, the target radiance component due to reflectance alone is found by subtracting the emitted component, which is calculated using the temperature of the target surface, integrating the Planck function and channel response function across the channel 3 bandwidth. The target temperatures were derived from AVHRR channels 4 and 5 via the split window technique (Sobrino et al. 1991; Ottle and Vidal-Madjar 1992), assuming cloud thermal emissivity equal to unity. The correction for thermal radiance was performed on a pixel-by-pixel basis, using the channels 3, 4, and 5 pixel values at each point. The resulting target temperature was checked against cloud-top temperatures we obtained during the in situ sampling. The LOWTRAN7 modeling produced the following calculations:

- downward direct solar flux, using the local solar zenith angle;
- upward transmittance along the path to the satellite sensor;
- path radiance upward along the satellite viewing angle; and
- downward diffuse flux to the cloud-top surface.

In each of the LOWTRAN7 calculations, we utilized a cloud-top altitude estimated by overlaying topographic contours on the terrain observable adjacent to the fog layer in the satellite images. This derived cloud-top altitude was verified at the study site from the tethersonde relative humidity profile. We assumed the LOWTRAN7 background tropospheric aerosol profile, which corresponds to 50-km visibility, above the inversion layer and a moderate, aged volcanic aerosol profile in the stratosphere. The atmospheric temperature and humidity profile were derived from the NOAA TOVS soundings obtained at the AVHRR image time in the area, after evaluating their correspondence to the closest National Weather Service (NWS) rawinsonde profile (1200 UTC 27 January, at Oakland).

In order to verify the calculations of upward path radiance, we developed a means of estimating the maximum path radiance in both channel 1 and channel 3. The sampled AVHRR channel 1 satellite-observed radiance over the cloud-free coastal ocean region produced minimum equivalent albedo values. Assigning this low albedo (0.04) to the ocean surface, it was assumed that the residual satellite-observed equivalent albedo was primarily contributed by atmospheric path radiance, and by converting the satellite pixel albedo to radiance, we put a maximum bound on the value of path radiance. The actual path radiance can be somewhat smaller in magnitude, due to the fact that path radiance from above the fog layer is expected to be less than that from the marine boundary layer upward. The same approach was used to estimate the path radiance in channel 3 but with the removal of thermal surface emission. In order to accomplish the correction for thermal emission, we utilized the split window technique for deriving surface temperature, the LOWTRAN7 calculated channel transmittance, and the Planck function to estimate the upward radiance due to the transmitted surface thermal signature. Again, this yields an upper bound for path radiance. These values corresponded within 10% to the LOWTRAN7 calculated path radiance values.

LOWTRAN7 sensitivity tests showed that atmospheric transmittance in the AVHRR channels could vary by 5% across the region simply as a result of a regional variation in precipitable water values, due to the long atmospheric path corresponding to low sun angle. While the impact of this on retrieved droplet size is small (less than a 1-μm-bias), the transmittance variation would cause approximately a 15% change in retrieved optical depth for the local conditions. The use of TOVS radiances for atmospheric correction was therefore evaluated. The TOVS soundings were con-

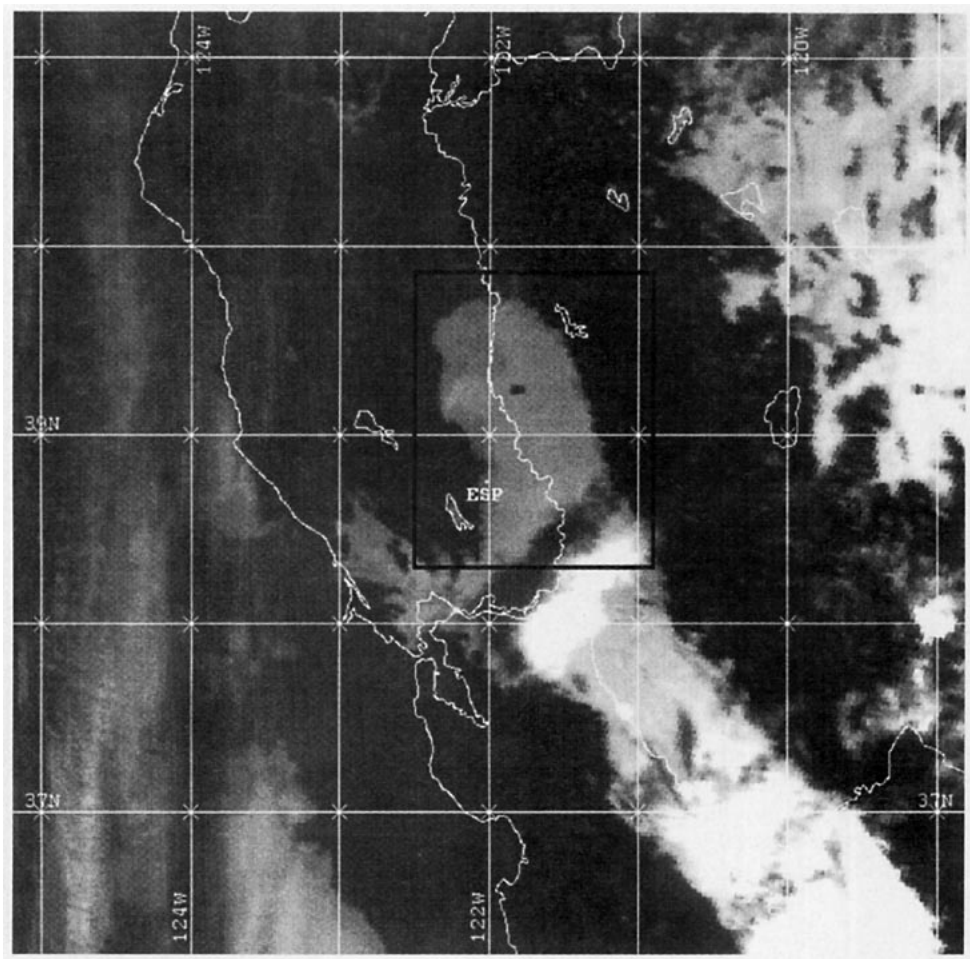

FIG. 8. AVHRR channel 1 image of central California and valley fog region on 27 January 1993. Note that an extensive area of fog also formed over the western Great Basin near Reno, Nevada.

sistent with NWS rawinsonde data obtained at 1200 UTC from a nearby station. The TOVS-derived precipitable water vapor field within our study region allowed us to make local correction to the above-cloud transmittance calculations. The hemispheric diffuse flux was calculated by angular integration over the sky hemisphere of LOWTRAN7 downward radiances. Use of reflectances calculated with Eq. (6) with model calculations of bidirectional reflectance assumes that the scattering of diffuse downward flux is characterized by the bidirectional scattering function for the direct solar beam. This assumption is valid to the extent that the downward diffuse flux is concentrated in the direction of the solar beam. The potential bias is small and decreases as cloud optical depth increases. A treatment that accommodates both satellite and model conditions for cloud bidirectional reflectance into the satellite view path from multiple angles of downward sky radiance would significantly increase computer time for operational retrievals. However, the recently developed MODTRAN3 code (Wang and Anderson 1994) may be useful in improving the specification of transmittance, path radiance, and diffuse flux for use in operational applications.

Following the determination of individual values of atmospheric transmittance, path radiance, and downward flux for channels 1 and 3 for the study region, these and the pixel target reflectances were stored in a geographic database with other point-specific parameters such as latitude, longitude, solar zenith angle, satellite view angle, sun–target–satellite relative azimuth angle, and surface temperature.

b. Retrieval of fog droplet size and optical depth

The radiative modeling parameters, after being derived and stored as discussed above, were then used to retrieve the cloud optical depth and droplet size and also used for displaying, plotting, contouring, and analyzing the results. The retrieval procedure follows these steps.

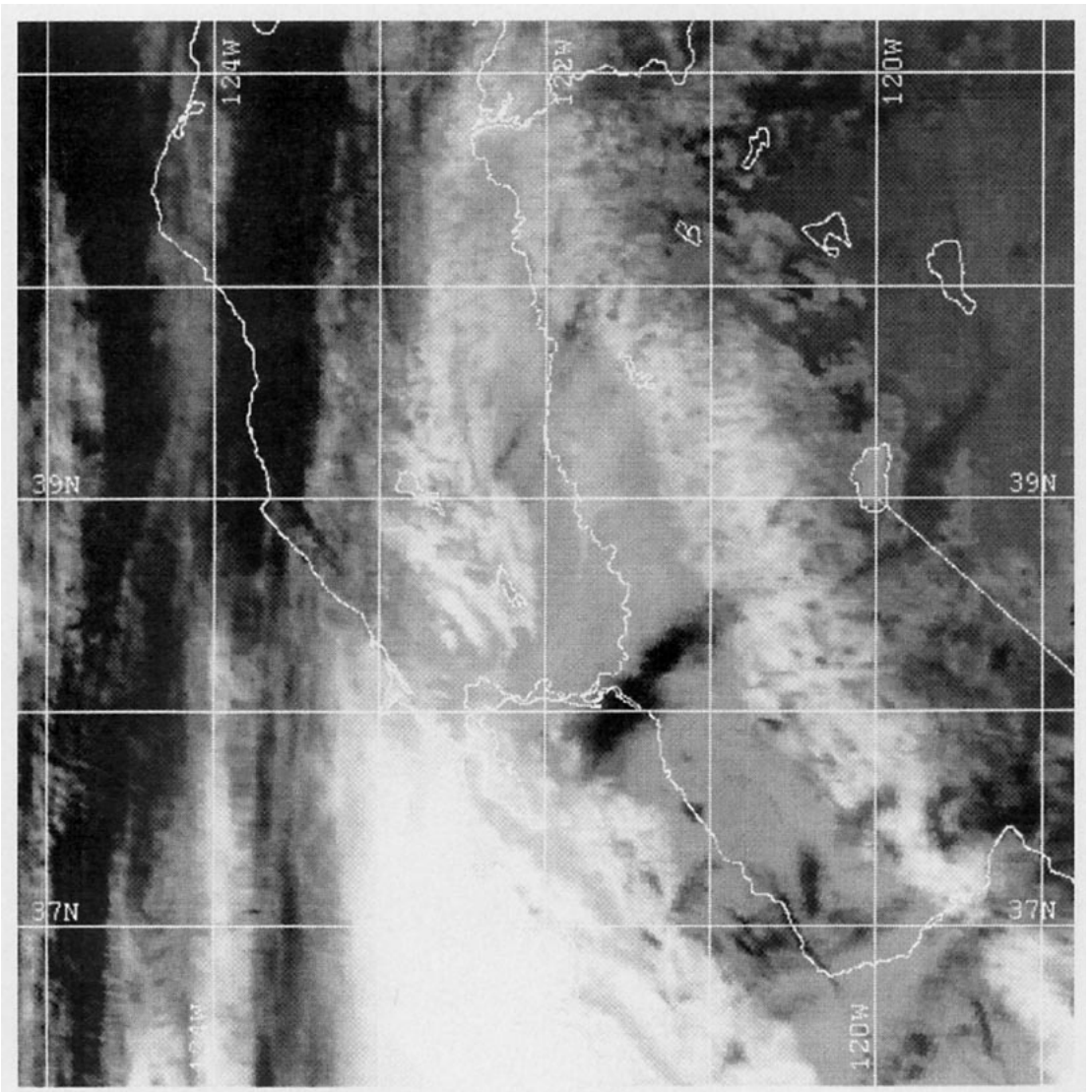

FIG. 9. AVHRR channel 4 image of central California, depicting cold (dark) cloud tops due to cirrus and altostratus, cool fog throughout the Central Valley, and warmer mountainous areas extending above the winter inversion layer.

1) Carry out calculations of the theoretical spectral reflectance for the expected cloud layers, including potential droplet size distributions and cloud depths.

2) Determine the appropriate solar zenith angle, satellite view angle, and relative azimuth angle for the region. These values may vary over an image analysis area if it covers a large geographic region.

3) Use a spline interpolation program to fit the derived two-channel reflectance pairs to the theoretical reflectance curves for a varied group of droplet size distributions. A bispectral spline interpolation, using the channel 1 and channel 3 reflectance values, provides a distinct separation of the channel 3 reflectances for clouds with channel 1 reflectance above an optical depth threshold (see Fig. 2).

4) Once an initial estimate of the droplet size distribution is made, the theoretical reflectance values for this type of cloud are used again to estimate the optical depth of that cloud. A second interpolation program is used to find the optical depth corresponding to the observed channel 1 reflectance.

5) The spatial distributions of the retrieved values of droplet size and optical depth are displayed in a geographically referenced format, allowing analysis of the spatial continuity and correspondence with other data parameters. Topographic contours are overlayed to estimate the areal distribution of cloud-top height in areas that impinge upon topography. Contours of the retrieved parameters themselves are overlayed to analyze the location and character of spatial features that may

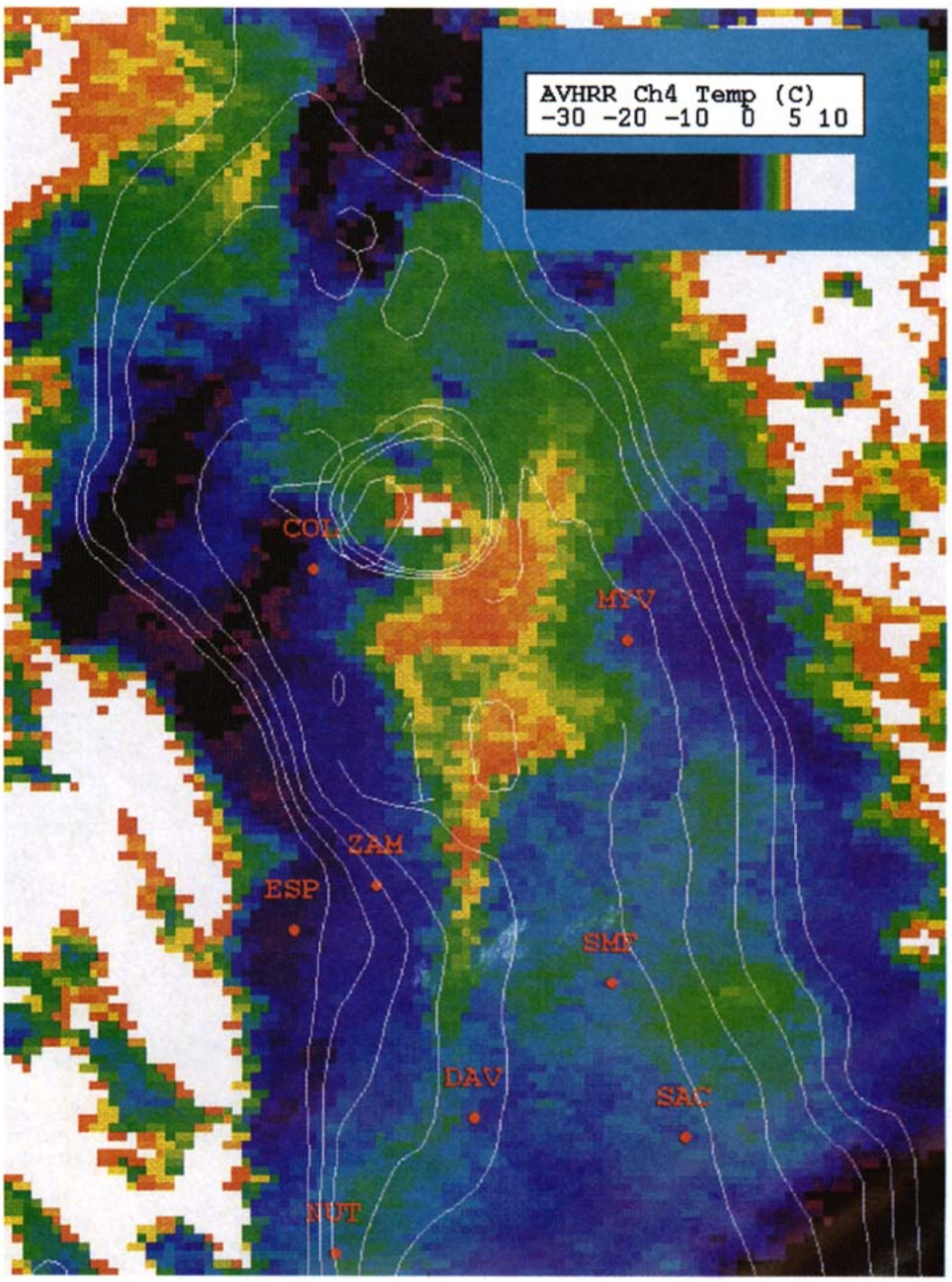

FIG. 10. High-resolution view of fog in northern Central Valley of California, with color-enhanced AVHRR channel 4 temperatures and graphic overlays of topographic contours (m, white) and surface observation sites (red). The clear-sky view of surrounding hillsides, which lie above the valley temperature inversion, shows as white (temperatures greater than 5°C). Thin cirrus bands cross the fog in the northwest and southeast corners of the image, which show as black (temperatures less than 0°C).

be related to the underlying topography or meteorological processes.

c. Case study of 27 January 1993

A calibrated AVHRR channel 1 image for this case is presented in Fig. 8, showing extensive fog cover within the Central Valley. A higher cloud layer crosses the fog near the river confluence at Sacramento and casts an extensive shadow over the fog layer to the north. The field study site (Esparto, California) is located a short distance farther north of the shadow region on the western side of the valley fog. Figure 9, a

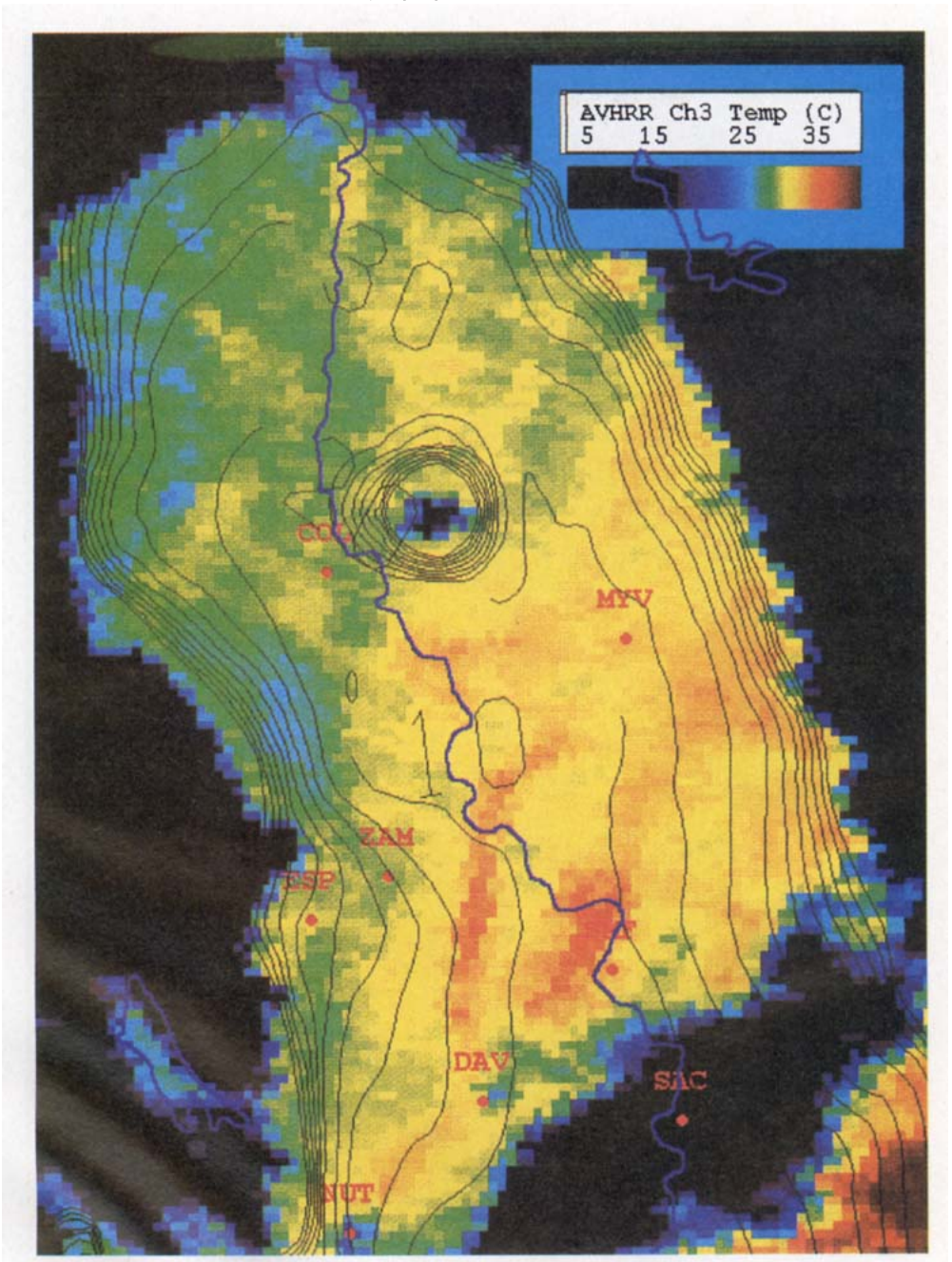

FIG. 11. High-resolution view of fog, corresponding to Fig. 9, for AVHRR channel 3. The color bar indicates the effective blackbody temperature of the pixels, which is the combined effect of reflected solar flux and emitted thermal radiance, where the solar contribution is dominant. Note the band of increased brightness located along the topographic gradient extending northward from the Nut Tree Airport (NUT) to Davis (DAV) and farther north. Graphic overlay of the river and lake features (blue) is also shown.

channel 4 (thermal window) image, clearly shows the colder (dark) high cloud crossing southwest–northeast over the central and northern regions of the valley fog and the brighter (warm) coastal mountain ridges to the west of the fog. Figures 10–12 are high-resolution calibrated images for AVHRR channels 4, 3, and 1, respectively, for the analysis area outlined in Fig. 8. The field observation site at Esparto (ESP) is indicated. The color-enhanced visible image in Fig. 12 shows a distance scale bar that applies to each of these images. Figure 10 provides the temperature distribution from AVHRR channel 4, with graphic overlay of topo-

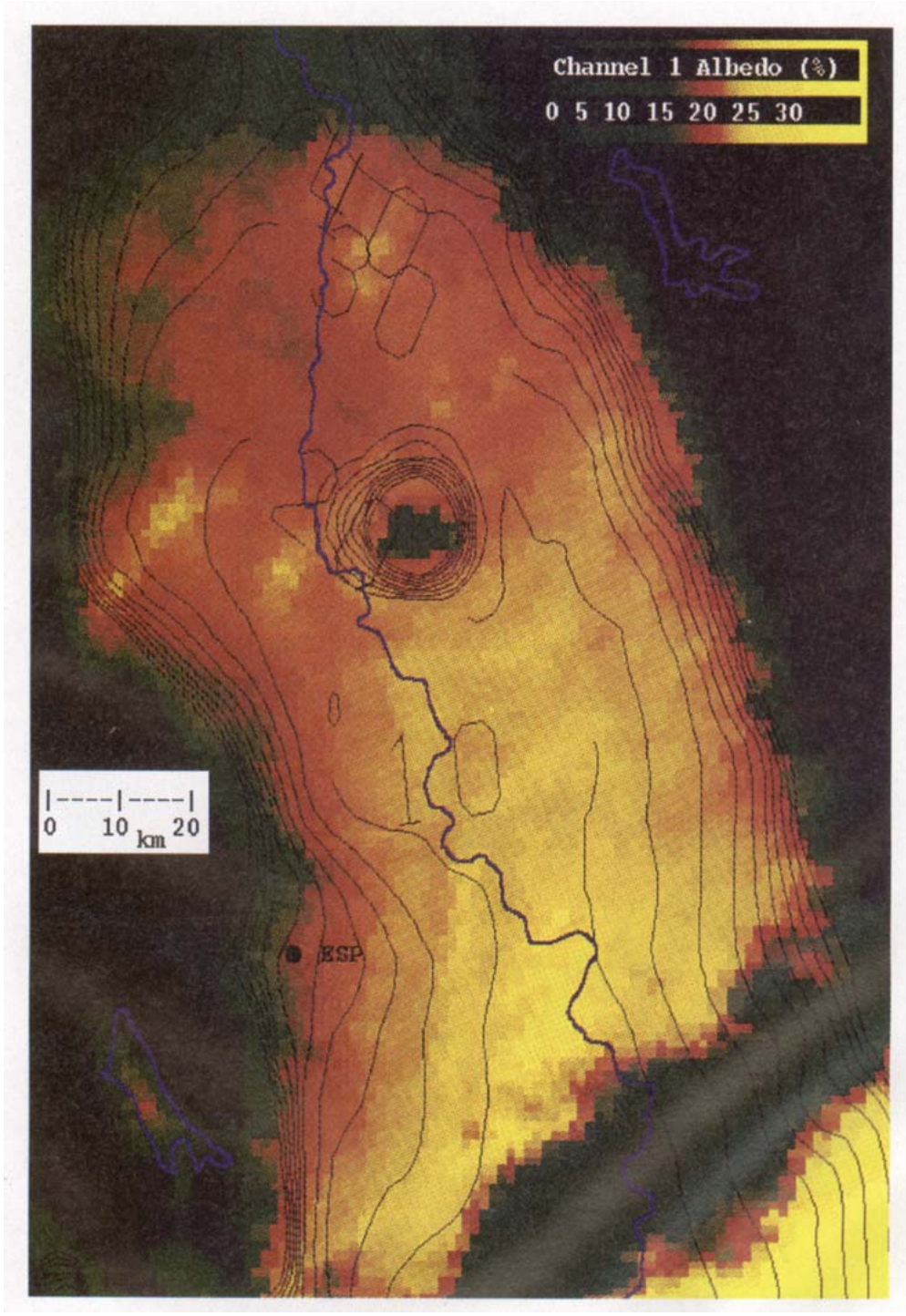

FIG. 12. High-resolution view in the AVHRR visible band (channel 1), with brighter color shading (red and yellow) indicating increasing equivalent albedo of the cloud area and green/blue/black indicating decreasing albedo in areas of cloud-free surface viewing (to the east and west of the fog area) and the shadow cast by an upper cirrus deck (in the southeast corner of the image). Graphic overlay of river and lake features (blue) and of topographic contours (m, black) are also shown.

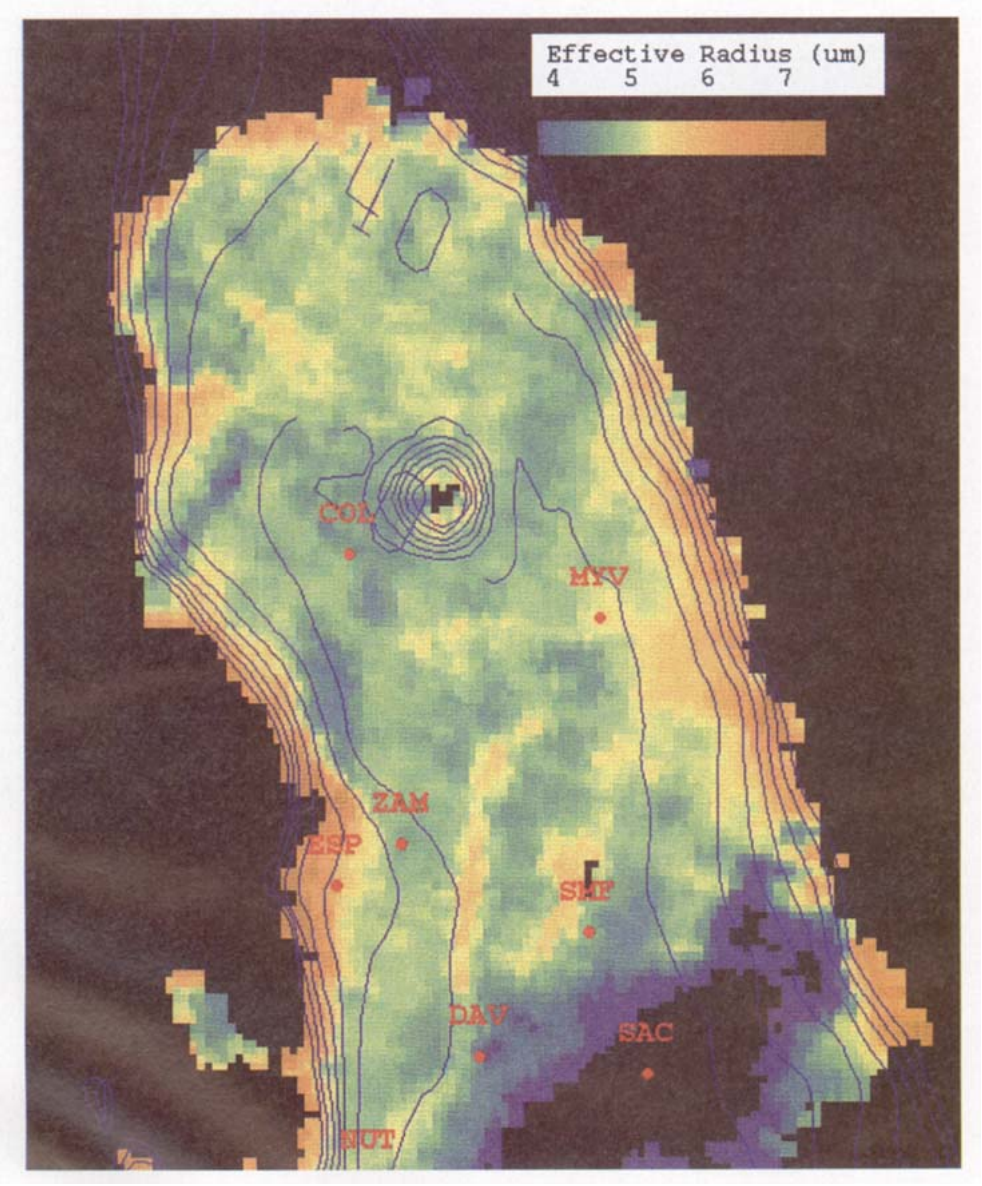

FIG. 13. Mapped distribution of retrieved droplet effective radius for the 27 January 1993 case.

graphic contours (10–50 m) that demonstrate the topographic influence on limiting the fog to the valley. The majority of the fog-top temperatures are 0°–2°C. Color enhancement indicates a slightly warmer fog top (3°–4°C) over the central area of the valley between Marysville (MYV) and Colusa (COL). The fog abuts a circular topographic obstacle (the volcanic Sutter Buttes) in the north central area of the valley fog, and the Buttes appear warmer (>5°C) due to their protrusion out of the fog into the inversion.

A narrow linear feature of warmer cloud top, oriented north–south, extends along the westward edge of the topographic gradient of the valley boundary. Comparison of this image with a channel 3 image (Fig. 11) shows a corresponding linear feature that indicates increased 3.7-μm radiance. From the channel 4 image in Fig. 10, it is apparent that a portion of the channel 3 brightness enhancement is due to thermal emission. The contribution by the blackbody-equivalent thermal emission is approximately 11% of the channel 3 total radiance, based on the cloud-top temperature retrieved from channels 4 and 5. Local enhancement of the near-infrared radiance is also likely due to increased reflectance, at least on the edge of the cloud facing the sun, as is indicated by the visible image brightness pattern of channel 1 (Fig. 12). The increased channel 3 brightness may be due to air convergence (as air flows along the sloping valley surface) and a resulting greater

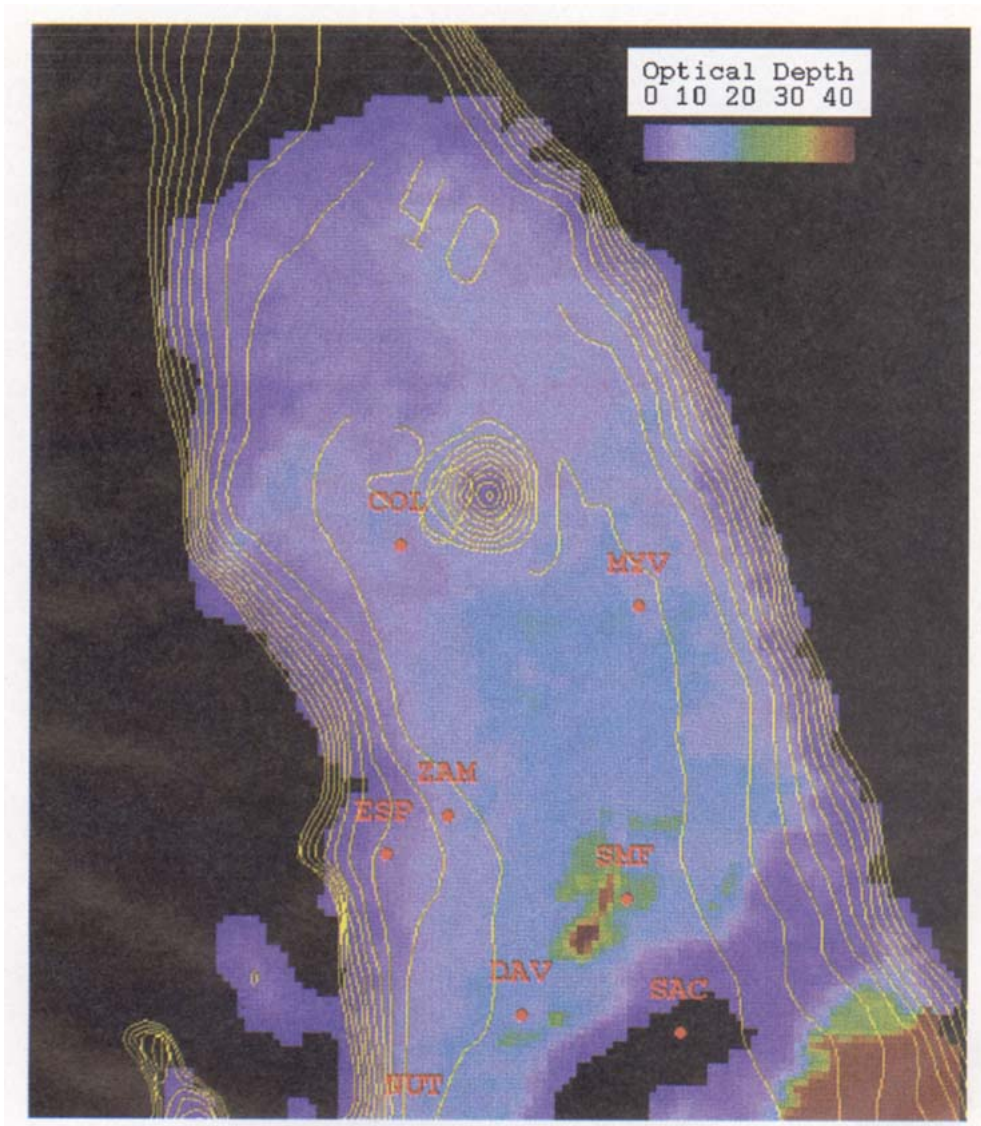

FIG. 14. Mapped distribution of retrieved optical depth for the 27 January 1993 case.

cloud-top height along this feature. A similar slight warming and brightening is seen near Sacramento (SMF). Cloud protrusion into the temperature inversion would produce a warming of cloud-top temperature, while at the same time allowing the low-angle solar beam to illuminate the cloud edge. Although an independent observation of the cloud-top surface structure was not available, the cloud-top protrusion is evidenced by the channel 1 image, which indicates a that a shadow is cast on the west (antisolar) side of the feature. The solar zenith angle for this image observation time would produce a shadow of length 870 m from a cloud protruding 200 m above the fog top, which would be sufficient to reduce the effective albedo in the AVHRR field of view if we assume that the shadowed area is approximately as reflective as that beneath the cirrus shadow. Because of the cloud shape effects on upwelling radiance, the parameter retrievals based on the plane-parallel model calculations are not completely appropriate for these localized cloud features. However, the majority of the fog area near the sampling area [ESP and Zamora (ZAM)] did appear to have a relatively uniform cloud-top surface, however.

The calculated results from the discrete ordinates multiple scattering model were used, for local scattering geometry conditions and the expected range of droplet size distributions, to estimate the fog optical depth and effective radius based on the retrieval procedure described in section 2. The retrieved values of fog droplet effective radius are relatively uniform over the fog area (see Fig. 13), with values in the range r_e

= 4.5–7.5 μm. The retrieved optical depth values are shown in Fig. 14 and generally lie in the range τ = 5–15. The values are similar to those observed at the field measurement site. The point values of these gridded retrieval results at the ESP field sampling location provide values of r_e = 6.1 μm and τ = 7, while the in situ fog profile measurements at Esparto produced a vertical average effective droplet radius value of r_e = 6.9 μm and total fog optical depth value of τ = 7. Large values of the effective radius retrieved over the north–south cloud feature noted earlier [passing Davis, California (DAV) and Nut Tree Airport (NUT)] may not be valid, due to the apparent cloud-top surface structure, but still lie within the majority of retrieved values for the fog area. However, convergence processes suggested by the cloud structure in that area may also be accompanied by changes in the droplet size distribution. The area of very high optical depth estimated near SMF is associated with high visible albedo and may be due in part to increased multiple scattering through the thin cirrus edge that is positioned directly to the southeast. The shadow feature from the cirrus is color-enhanced as a green southwest–northeast band in the lower left corner of the channel 1 image (Fig. 12). There are also indications of thin cirrus overlying the northwestern valley fog area, as evidenced by colder temperatures in channel 4 (Fig. 10), slightly higher equivalent temperatures in channel 3 (Fig. 11), and small bands with higher visible brightness (Fig. 12). These, if not screened out of the retrieval process, produce pixel estimates corresponding to smaller droplet size (Fig. 13) and larger optical depth (Fig. 14).

A scattergram of the derived cloud reflectances (Fig. 15) is plotted with the theoretical model results for clouds of varying droplet effective radius. A distinct cluster of observations is seen between the curves corresponding to droplet sizes of 6 and 9 μm. Some of these points extend into the diagram region of much higher reflectances. This behavior can occur due to nonplane parallel cloud structure, in which the satellite observes radiation scattered from cloud edges. The central value of cloud droplet effective radius for this scattergram is approximately r_e = 7.0 μm. Other clusters on this scattergram are two "feet" of low reflectance rising from surface albedos near 10% and 30%, corresponding to bare ground, and the fog lying under the high cloud shadow, respectively. Land and cloud pixels are shown together here to emphasize the manner in which bispectral reflectances are influenced by their illumination and pixel composition. The inferred shadow area pixel cluster extending from the 30% channel 1 reflectance remains distinct up to a value of 60%, where it appears to merge with the fog cluster. Pixel space between the various clusters can be interpreted as fields of view along target edges, and objective threshold techniques should utilize the actual scattergrams on a case basis to group pixel types.

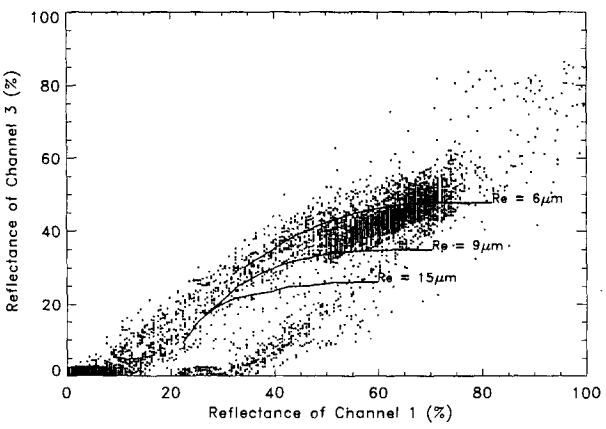

FIG. 15. Scattergram of derived bispectral reflectances and model results for three different fog droplet size distributions.

d. Simulation of GOES-8 *observations*

In anticipation of the spring 1994 launch of GOES-I (which was successful and is now providing data as *GOES-8*), we used the AVHRR data to simulate the improved (4 km) resolution of the *GOES-8* near-infrared and thermal channels. Of course, today we may use the *GOES-8* and *GOES-9* observations directly (Kleespies 1995). In order to produce the simulated data, a 4 km × 4 km resolution dataset was created by subsampling the AVHRR image channels, and we then applied the droplet size retrieval procedure on this 4-km data. For comparison, the retrieved droplet size for AVHRR maximum resolution is shown first in Fig. 16a, followed by the *GOES-8* simulated retrieval in Fig. 16b. The obvious differences are the loss of small-scale patterns, which are associated with cloud macrophysical structure, and the loss of a distinct transition along the topographic features.

By comparing histograms for the retrieved droplet size in each of these datasets (Figs. 17a,b), we find the 1-km pixel results are more uniformly distributed about a mean value of $r \approx 6.8$ μm. The histogram for the 4-km pixel resolution has a smaller distribution tail for $r_e > 7$ μm and a mean value for effective radius of $r_e \approx 6.2$ μm. The *GOES-8* simulated data has produced values that are smaller by approximately 0.7 μm. This suggests that the reduced field of view causes the near-infrared radiance to be reduced proportionally less than that of the visible channel. By utilizing the 1-km GOES visible data to find a maximum pixel brightness within the near-infrared field of view, it may be possible to obtain a bispectral signature similar to the 1-km AVHRR data.

6. Application to visibility monitoring

One of the potential applications for remote sensing of fog physical structure is the estimation of visibility

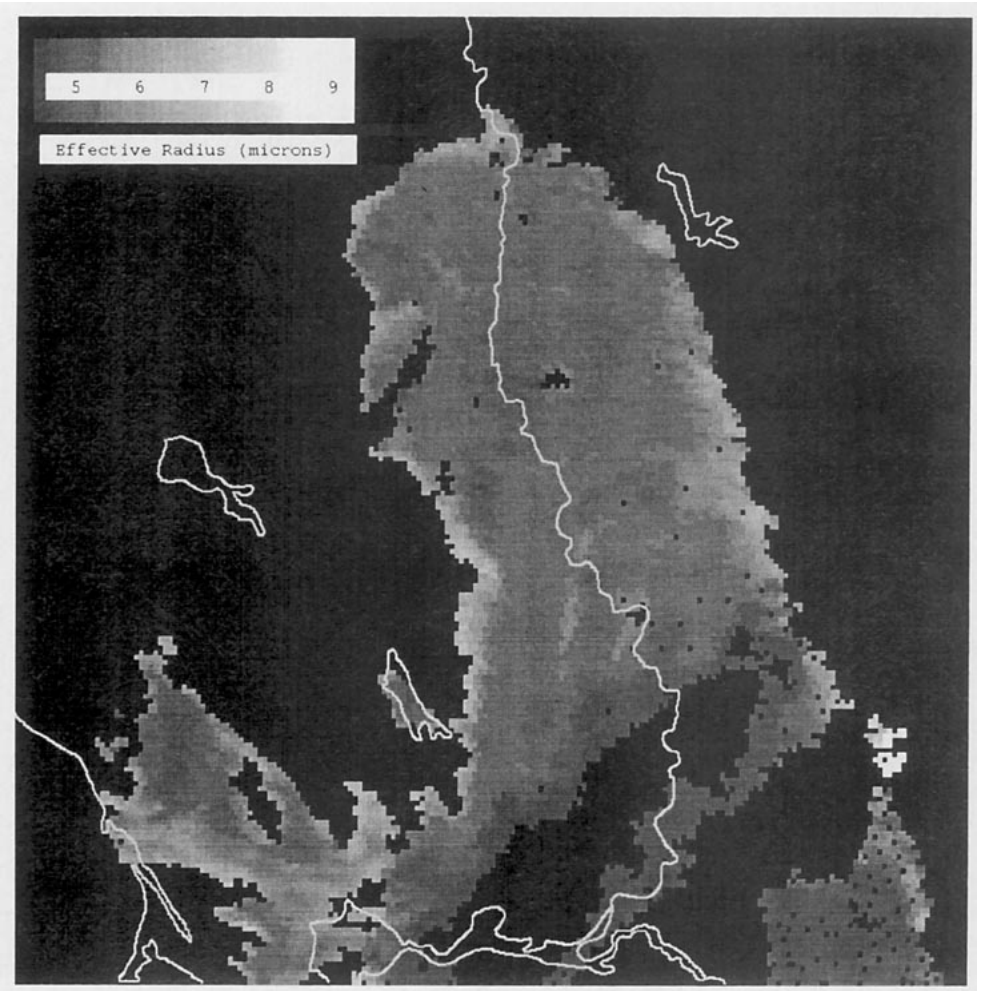

FIG. 16a. Estimated droplet effective radius field, derived from the full resolution AVHRR data for comparison to the simulated *GOES-8* 4-km data.

conditions and the quantitative measure of those conditions, the visual range (VR). Visual range is defined as the maximum distance at which the human eye can distinguish an object. During daytime, the visual range is determined by the reflectivity or albedo of the target (A_t), as well as the background (A_b), and the radiative extinction coefficient (k) between the target and the eye, following the equation (Berry et al. 1945):

$$\mathrm{VR} = \frac{1}{k} \ln\left[\frac{1}{\epsilon}\left(\frac{|A_t - A_b|}{2} + \epsilon - \frac{\epsilon A_t}{2}\right)\right], \quad (7)$$

where ϵ is the minimum fractional contrast recognizable to the human eye over the visible wavelength range (400–740 nm), typically assumed to be 0.1–0.2. The wavelength for which the extinction coefficient and contrast are calculated is generally taken to be 0.55 μm, where the human eye has peak sensitivity to incoming light. The background albedo is a function of the droplet population of the fog, and depending on the line of sight and whether the fog is optically thin, it is also a function of the background vegetation or buildings that may be present in the scene. The fog background albedo will be related to the local extinction coefficient as well as the fog optical depth and angular pattern of diffuse scattering. The target albedo is determined by the target surface itself, such as an automobile with illuminated headlights, a road barrier, a deer, etc. The visual range can be used to establish highway speeds that provide a safe stopping distance.

Background albedo for a given fog layer can be calculated from the DISORT model that was utilized in the present study. In the case of applications to transportation hazard warnings, it can be assumed that the viewing path is short, so that horizontal variations are small. Given an assumed vertical profile (homogeneous or layered) of the fog droplet size distributions, DISORT will produce the angularly dependant background albedo. The fog background reflectance pattern is most variable at forward and backward scattering

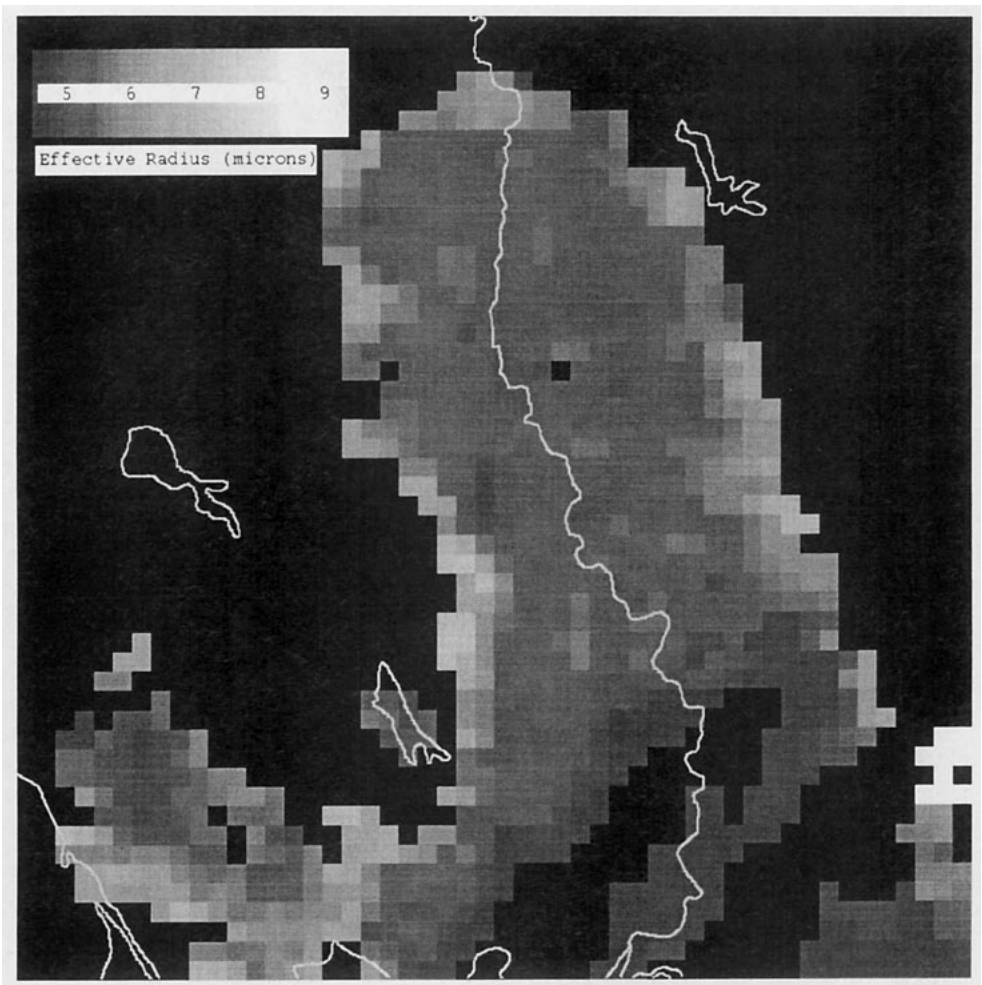

FIG. 16b. Estimated droplet effective radius field, using the simulated *GOES-8* data in the AVHRR retrieval method.

directions in early morning due to low solar elevation angle. The angular pattern of scattered sunlight becomes increasingly isotropic as fog optical depth increases.

Extinction along a viewing path is determined by the values of the extinction coefficient of the droplet population. Therefore, the estimation of visual range ideally requires a path-dependant method that accounts for both horizontal and vertical variations in droplet size. The use of satellite remote sensing to estimate droplet size (and fog optical and physical depths) from cloud-top radiances, in addition to a phenomenological or numerical simulation model for the vertical variation in droplet size distribution, could provide more information on location-specific visual range than is currently obtained from any observations.

The vertical structure of fog layers has been examined in a variety of field and model studies. Kunkel (1982) has made fog droplet size observations for 12 case studies and found that extinction coefficients were consistently higher at an altitude of 30 m than at 5 m above ground, due to increased number concentrations and liquid water contents, while mean droplet size was relatively invariant with height. Similar results were found for the case study we have described in this paper. Kunkel found that while the various droplet size distributions often had large concentrations of haze-size (radius less than 2 μm) particles, they contributed less than 5% to the total extinction in the fog. These observations suggest that satellite-derived cloud droplet effective radius may adequately characterize droplet size near the surface, but that additional information may be needed to characterize the vertical profile of extinction. Second, the retrieved value of optical depth, adjusted for a "typical" or model-derived vertical profile of liquid water content (and providing extinction coefficient), may then be applied to radiative transfer calculations to estimate the near-surface visual range. The entire procedure can be accomplished on a microcomputer,

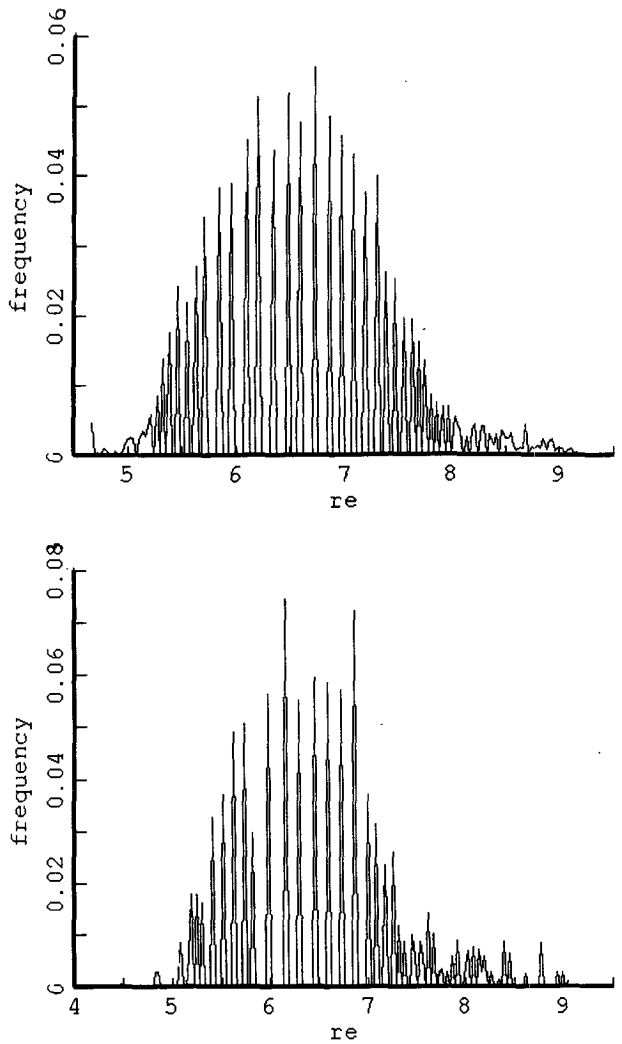

FIG. 17. (a) Histogram of effective radius values retrieved for the full-resolution AVHRR data, over the northern portion of the fog area (within the white box outline shown in Fig. 16). (b) Histogram of effective radius values retrieved for the simulated *GOES-8* 4-km data, in the same area as (a).

using database files of lookup tables derived from prior calculations for a given sun–target–satellite viewing geometry.

Visual range in fog at night is generally dependant on the brightness of an illuminated target, such as automobile or aircraft lights, and the local extinction coefficient. Estimation of visual range from nighttime satellite observations would require use of the thermal radiance signature in the AVHRR 3.7- or GOES 3.9-μm and 10–12-μm bands and is not addressed in this paper. However, it is recommended for future studies in order to extend fog nowcasting capabilities to a 24-h cycle, which could be particularly helpful during the formation and growth phases of nocturnal fog. At the present time, techniques have been developed for identifying the presence of fog, utilizing the temperature difference between the near-infrared and thermal channels of AVHRR and GOES (Ellrod 1995). Extension to droplet size, optical depth, and visual range estimates at night may be possible but are likely to be more sensitive to the knowledge of surface thermal emission than is the daytime analysis technique described here and, hence, may require enhanced surface observational data, such as the measurements of soil moisture made by agricultural mesonetworks.

7. Concluding discussion

A methodology has been developed for the remote sensing retrieval of droplet size and optical depth for land-based fog. The NOAA AVHRR multispectral image data were applied to this procedure and produced results consistent with observations and analysis of fog occurring in the Central Valley area of California. The AVHRR data were also utilized to compare these retrievals to those from simulated *GOES-8* data, and it was concluded that the collocation of the GOES 1-km visible data should be used in interpretation of the estimates of droplet size at the 4-km resolution of the *GOES-8* 3.9-μm channel. The mapping of fog droplet size and optical/physical depth on a global basis, by including methods for land-based fogs, has applications ranging from earth radiation budget monitoring (Boucher 1995) and cloud–climate feedback studies {e.g., NASA EOS [Earth Observing System] and ISCCP FIRE [First ISCCP (International Satellite Cloud Climatology Project) Regional Experiment] satellite programs} to the design of optimal sampling methods for "harvesting" fog water (Schemenaur and Cereceda 1992).

Analysis of the AVHRR case studies has allowed us to identify two potential improvements to the retrieval procedures. First, the 27 January case included areas where high cloud casts shadow on the lower fog layer, and this shadow is large in area due to the low morning sun zenith angle. Clear–cloudy discrimination tests must include the possibility of shadow areas. While the lack of reflected sunlight may prevent parameter retrieval, multispectral combinations may be able to correctly identify fog area even when reflectance of channels 1 and 2 is below preset thresholds. Persistance of the upper cloud deck also may be due to the relatively cold radiating temperature of the fog (near 0°C) compared to surrounding terrain, which slows the cloud-base warming.

A second observation regarding the retrieval method is that topographic variability below fog influences observed radiances, such as those along the topographic gradients (slopes) and those due to airflow. Thus, merging of satellite and topographic databases allows more thorough evaluation of mesoscale cloud retrieval results. In addition, it is often possible to estimate fog physical depth from the closest topographic contour of

clear pixels. The operational implementation of the fog microphysical retrieval method requires the development of a geographic database in which information on surface conditions and meteorological observations is accessed. As each AVHRR image is processed on a daily basis, a clear–cloudy determination is made, and surface conditions such as albedo and emissivity can be deduced.

Finally, we note that the value of the early morning AVHRR overpass time for cloud retrievals is limited by the low sun angle, which reduces cloud reflectance characteristics and increases the uncertainties in the flux of direct and diffuse radiation to the cloud top. It is recommended that the morning overpass time be moved later by one hour on future NOAA satellites to allow useful fog observations during both winter and summer. It is felt that the information gained on morning cloud and fog characteristics may outweigh the loss of other observations, such as late afternoon/early evening cloud cover.

Acknowledgments. This research was supported by the NOAA Office of Global Programs under Grant NA26GP0058-02, as well as the NASA Space Grant Program of the University and Community College System of Nevada. The instrument engineering contributions by Richard Purcell, Harold Faretto, and Paul Lage of the Desert Research Institute are very gratefully acknowledged. In addition, we extend our thanks to the Durst family for allowing us to conduct the fog profile sampling at their farm near Esparto.

REFERENCES

Berry, F. A., Jr., E. Bollay, and N. R. Beers, Eds., 1945: *Handbook of Meteorology.* McGraw-Hill, 1068 pp.

Bott, A., U. Sievers, and W. Zdunkowski, 1990: A radiation fog model with a detailed treatment of the interaction between radiative transfer and fog microphysics. *J. Atmos. Sci.,* **47,** 2153–2166.

Boucher, O., 1995: GCM estimate of the indirect aerosol forcing using satellite-retrieved cloud droplet effective radii. *J. Climate,* **8,** 1403–1409.

Duynkerke, P. G., 1991: Radiation fog: A comparison of model simulation with detailed observations. *Mon. Wea. Rev.,* **119,** 324–341.

Ellrod, G. P., 1995: Advances in the detection and analysis of fog at night using GOES multispectral infrared imagery. *Wea. Forecasting,* **10,** 606–619.

Kidwell, K. B., 1991: NOAA polar orbiter users guide. 137 pp. [Available from NOAA Satellite Data Services Division, Washington, D.C. 20233.]

Kleespies, T. J., 1995: The retrieval of marine stratiform cloud properties from multiple observations in the 3.9-μm window under conditions of varying solar illumination. *J. Appl. Meteor.,* **34,** 1512–1524.

Kneizys, F. X., E. P. Shettle, L. W. Abreu, J. H. Chetwynd, G. P. Anderson, W. O. Gallery, J. E. A. Selby, and S. A. Clough, 1988: Users Guide to LOWTRAN7. Envir. Res. Pap. 1010, AFLG-TR-88-0177, 137 pp. [Available from Air Force Geophysics Laboratory, Hanscom AFB, MA 01731.]

Kunkel, B. A., 1982: Microphysical properties of fog at Otis AFB, AFGL-TR-82-0026, AD A119928, Air Force Geophysics Laboratory, Hanscom AFB, MA, 113 pp.

Lee, T. F., 1987: Urban clear islands in California Central Valley fog. *Mon. Wea. Rev.,* **115,** 1794–1796.

Marple, V. A., and K. Willeke, 1976: Impactor design. *Atmos. Environ.,* **10,** 891–896.

Nakajima, T., M. D. King, J. D. Spinhirne, and L. F. Radke, 1991: Determination of the optical thickness and effective particle radius of clouds from reflected solar radiation measurements. Part II: Marine stratocumulus observations. *J. Atmos. Sci.,* **48,** 728–750.

Okland, H., and Y. Gotaas, 1995: Modelling and prediction of steam fog. *Beitr. Phys. Atmos.,* **68,** 121–131.

Ottle, C., and D. Vidal-Madjar, 1992: Estimation of land surface temperature with NOAA-9 Data. *Remote Sens. Environ.,* **40,** 27–41.

Pandis, S. N., and J. H. Seinfeld, 1989: Mathematical modeling of acid deposition due to radiation fog. *J. Geophys. Res.,* **94**(D10), 12 911–12 923.

——, ——, and C. Pilnis, 1990: The smog-fog-smog cycle and acid deposition. *J. Geophys. Res.,* **95**(D11), 18 489–18 500.

Pincus, R., M. Szczodrak, J. Gu, and P. Austin, 1995: Uncertainty in cloud optical depth estimates made from satellite radiance measurements. *J. Climate,* **8,** 1453–1462.

Platnick, S., and S. Twomey, 1994: Determining the susceptibility of cloud albedo to changes in droplet concentration with the Advanced Very High Resolution Radiometer. *J. Appl. Meteor.,* **33,** 334–347.

——, and F. P. J. Valero, 1995: A validation of a satellite cloud retrieval during ASTEX. *J. Atmos. Sci.,* **52,** 2985–3001.

Schemenauer, R. S., and P. Cereceda, 1992: The quality of fog water collected for domestic and agricultural use in Chile. *J. Appl. Meteor.,* **31,** 275–290.

Sobrino, J. A., C. Coll, and V. Caselles, 1991: Atmospheric correction for land surface temperature using NOAA-11 AVHRR channels 4 and 5. *Remote Sens. Environ.,* **38,** 19–34.

Stamnes, K., and L. Swanson, 1981: A new multi-layer discrete ordinate method for radiative transfer calculations in anisotropically scattering atmospheres. *J. Atmos. Sci.,* **38,** 387–399.

——, S. C. Tsay, W. Wiscombe, and K. Jayaweera, 1988: A numerically stable algorithm for discrete-ordinate-method radiative transfer in multiple scattering and emitting layered media. *Appl. Opt.,* **27,** 845–862.

Taylor, J. P., 1992: Sensitivity of remotely sensed effective radius of cloud droplets to changes in LOWTRAN version. *J. Atmos. Sci.,* **49,** 2564–2569.

Tonna, G., 1989: Physical and optical properties of fog at 74 wavelengths from 0.35 to 90 μm with a sample of 239 spectra. *J. Meteor. Soc. Japan,* **67,** 5–8.

Tsay, S.-C., K. Stamnes, and K. Jayaweera, 1990: Radiative transfer in stratified atmospheres: Development and verification of a unified model. *J. Quant. Spectrosc. Radiat. Transfer,* **43,** 133–148.

Twohy, C. H., P. A. Durkee, B. J. Huebert, and R. J. Charlson, 1995: Effects of aerosol particles on the microphysics of coastal stratiform cloud. *J. Climate,* **8,** 773–783.

Wang, J., and G. P. Anderson, 1994: Validation of FASCOD3 and MODTRAN3: Comparison of model calculations with interferometer observations from SPECTRE and ITRA. *Proc. of Passive Infrared Remote Sensing of Clouds and the Atmosphere II,* Rome, Italy, SPIE, 220–231.

Welch, R. M., and B. A. Wielicki, 1986: The stratocumulus nature of fog. *J. Climate Appl. Meteor.,* **25,** 101–111.

——, M. G. Ravichandran, and S. K. Cox, 1986: Prediction of quasi-periodic oscillations in radiation fogs. Part I: Comparisons of simple similarity approaches. *J. Atmos. Sci.,* **43,** 633–651.

Wetzel, M. A., and T. H. Vonder Haar, 1990: Remote sensing of cloud droplet effective radius. Preprints, *Seventh Conf. on Atmospheric Radiation,* San Francisco, CA, Amer. Meteor. Soc., 277–283.

——, and ——, 1991: Theoretical development and sensitivity tests of a stratus cloud droplet size retrieval method for AVHRR-K/L/M. *Remote Sens. Environ.,* **36,** 105–119.

Wobrock, W., G. Kramm, and F. Herbert, 1986: The influence of the aerosol distribution and composition on the formation and evolution of radiation fog. *AEROSOLS: Formation and Reactivity,* J. Israel, Ed., Pergamon Journals Ltd., 426–429.

Zuidema, P., and D. L. Hartmann, 1995: Satellite determination of stratus cloud microphysical properties. *J. Climate,* **8,** 1638–1657.